Li and Na metal ion-induced defects in CuO nanocrystallites studied by positron annihilation spectroscopy

S. Sellaiyan[1] · P. Ajaykumari[2] · L. Vimaladevi[3] · M. Avinash[2] · A. Subbiah[4] · K. Sivaji[2]

Abstract

Alkali metal ion (Li^+ and Na^+)-doped CuO nanocrystallites were investigated using X-ray diffraction (XRD), transmission electron microscopy (TEM), positron annihilation lifetime (PAL), and Doppler broadening annihilation radiation (DBAR) spectroscopy methods. A comparative analysis of XRD, TEM, average lifetime, and electron momentum variation is presented based on defect formation and curing. DBAR studies divulge the positron trapping sites as Cu vacancies and vacancy complex clusters in undoped CuO. The study also reveals lattice defect and migration of point defect in the doped CuO lattice. The positron lifetimes of undoped CuO show extended point defects, V_{Cu}–V_O vacancy complexes, and voids. These defects are reduced to Cu interstitial (Cu_i) type point defects upon annealing. The lifetime confirms the V_{Cu} recovery and cluster vacancies for annealed Li- and Na-doped CuO. Higher Li concentrations showed a significant point defect of isolated oxygen vacancies as well as Li interstitials. Antisite and oxygen interstitial-type defects are prominent for all the Na concentrations.

Keywords Alkali metal-doped CuO · Defects · Positron lifetime · Doppler broadening

1 Introduction

Copper oxide (CuO) nanoparticles are broadly used in optical, catalysis, and many more research areas in modern technologies [1, 2]. The defect in oxide materials determines material properties and usefully modifies their physical properties [3–6]. Defect-related electrical and thermal properties of Li-, Na-, and K-doped CuO was investigated for use as a thermoelectric material [7]. In particular, vacancy, vacancy cluster, and grain boundary defects alter or enhance the material's properties. The addition of impurity ions (similar or different ionic radii) also creates defects in the lattice and affects the lattice planes in terms of the impurity concentration [8]. The synthesis condition and the morphology of the material resolve the changes in the concentration of defects type [9].

The synthesis and characterization of copper oxide nanostructures were studied extensively owing to their interesting characteristics [10, 11]. The effects of doping transition metal ions (In^{3+}, Mn^{3+}, Fe^{3+}, Ni^{2+}, Zn^{2+}) into the CuO lattice were reported [12, 13]. When the Cu^{2+} ion of the CuO lattice is substituted by alkali metals, the creation of oxygen vacancies is predominant to keep the CuO matrix neutral [14, 15]. Although there are various methods for the synthesis of CuO nanoparticles [16, 17], the main concern is the size, toxicity, and stability of the particles. In addition, a large quantity of the material can also be prepared by low-cost solution combustion synthesis method; however, defects and concentration are extremely high [17, 18]. The defect nature, defect modification, alkali metal ion concentration, and the annealing behavior of doped CuO are necessary for devices. Experimental evidence of the vacancy defects of alkali metal-doped MgO, rare earth metal-doped CuO and co-doped ZnO studied by positron annihilation are reported [19–21].

Positron annihilation is a well-established technique for the study of atomic-scale defects in solids [22, 23]. The annihilation characteristics such as lifetime or momentum/energy changes, when positrons (e +) are associated with

✉ S. Sellaiyan
  selva2d@gmail.com; sellaiyan.selvaku.gb@u.tsukuba.ac.jp

[1] Division of Applied Physics, University of Tsukuba, Ibaraki 305-8573, Japan

[2] Department of Nuclear Physics, University of Madras, Guindy Campus, Chennai 600025, India

[3] Department of Physics, Anna University, MIT Campus, Chennai 600044, India

[4] CSIR-Central Electrochemical Research Institute, Karaikudi, Tamil Nadu 630003, India

electrons (e-), trapping at defects site and at free-volume type defects enable to detection and characterize defect's nature. This technique represents a versatile probe for the study of atomic-scale defects, free-volume type defects, lattice vacancies, vacancy agglomerates, open-volume defects which can support understand their physical behavior and microstructural origins. The quantitative description of the annihilation characteristics in grain boundaries and interfaces is most important since the diffusion limitation of the trapping process [24]. The different charge states and size of vacancies can be distinguished from the change in positron lifetimes [25, 26]. Trapped positrons in the defects due to low electron density exhibit a longer lifetime than untrapped positrons lifetime. Positron Doppler broadening reveals information about weakly bound valence electrons and tightly bound core electrons, which contribute to the low- and high-momentum distributions [27]. Defects in metals, semiconductors, and polymers at the atomic scale are widely studied using positron annihilation lifetime (PAL) and Doppler broadening of the annihilation radiation (DBAR) spectroscopy [28]. Positron lifetime studies are used for quantitative information on defect type, size, and defect concentration. Electron momentum variations (by DBAR) deduce the defect type and concentration at the site of positrons in addition to the chemical environment around the defects.

The present study is aimed at identifying the nature of defects in solution combustion synthesized Li-doped and Na-doped CuO nanostructures using PAL and DBAR spectroscopies. The defects formations as a function of dopant concentration, migration of defect species, and recovery or modification of defects with annealing are of importance in technological development. On this aspect, the impact of lattice defects on the physiochemical properties is important to explore the role of impurities that interact with native defects and lead to the material properties modification at the nanoscale. Moreover, the impact of specific defects on the electronic properties of alkali-doped CuO is still a subject of interest. Hence, the present study focuses on the defect type modification, the defect concentration effect, and the effect of Li, Na alkali ion dopants and the annealing effect behavior in CuO nanostructures.

2 Experimental

The solution combustion technique was used to synthesize CuO and alkali (Li, Na)-doped CuO nanopowders. Copper nitrate ($Cu(NO_3)_2.3H_2O$) was selected as an oxidizer and glycine (NH_2CH_2COOH) was used as fuel for the preparation of CuO nanostructures. Lithium nitrate ($LiNO_3$) and sodium nitrate ($NaNO_3$) were used as an oxidizer for preparing Li- and Na-doped CuO according to the procedure of $Cu_{1-x}Li_x/Na_xO$ ($x = 0$, 0.01, 0.03 and 0.05). The stoichiometric composition of oxidizers and fuel was dissolved properly by 45-min stirring and transferred to a 100 °C preheated electric mantle. This resulted in a black color powder that was grounded well for a fine texture and calcined to 400 °C to remove the residues such as nitrates, organic additives, etc. and considered as as-prepared undoped and doped samples. Further, parts of the prepared samples were annealed at 800 °C to study the annealing effect.

Powder X-ray diffraction pattern was recorded by Seifert X-ray diffractometer (XRD) using Cu-Kα_1 radiation (1.5406 Å) to determine the $Cu_{1-x}X_xO$ (X = Li, Na) nanoparticle crystal structure and the crystallites size. Crystalline quality, morphology, and electron diffraction pattern were performed using an HRTEM equipped with a SAED of model G2 F20 (FEI Netherland). The PAL spectra were recorded for a cumulative count of 4×10^6 for all the samples using a conventional lifetime spectrometer with a digital storage oscilloscope. The measured lifetime spectra were deconvoluted with multiple exponential components to resolve various lifetime parameters. The spectra were analyzed with an experimental time resolution of 190 ps using the RESOLUTION program [29]. DBAR momentum spectrum was measured from the high-resolution energy signals derived from a conventional HP-Ge detector following the process of nuclear spectroscopy techniques and stored as a histogram. The characteristic 511 keV annihilation photopeak with an energy resolution of ~ 1.2 keV with a channel width of 0.071 keV was used. A sum of 10×10^7 counts in the annihilation peak was collected to derive the S (shape) and W (wing) parameters by an analysis method. The two comparable parameters extracted from the central and wing portions of the energy spectrum are the annihilation from the valance electron denoted as the S parameter and the annihilation from the core electrons denoted as the W parameter. The detailed experimental procedures and the instrument of PAL and DBAR spectroscopy have been explained in our previous reports [21].

3 Results and discussion

3.1 XRD and HRTEM

The XRD pattern of as-prepared (400 °C) and annealed (800 °C) undoped, Li-doped, Na-doped CuO samples shown in Fig. 1, exhibits a distinct monoclinic phase of CuO nanostructures. The modified peak width and intensity of the XRD pattern evidenced the addition of alkali metal ions
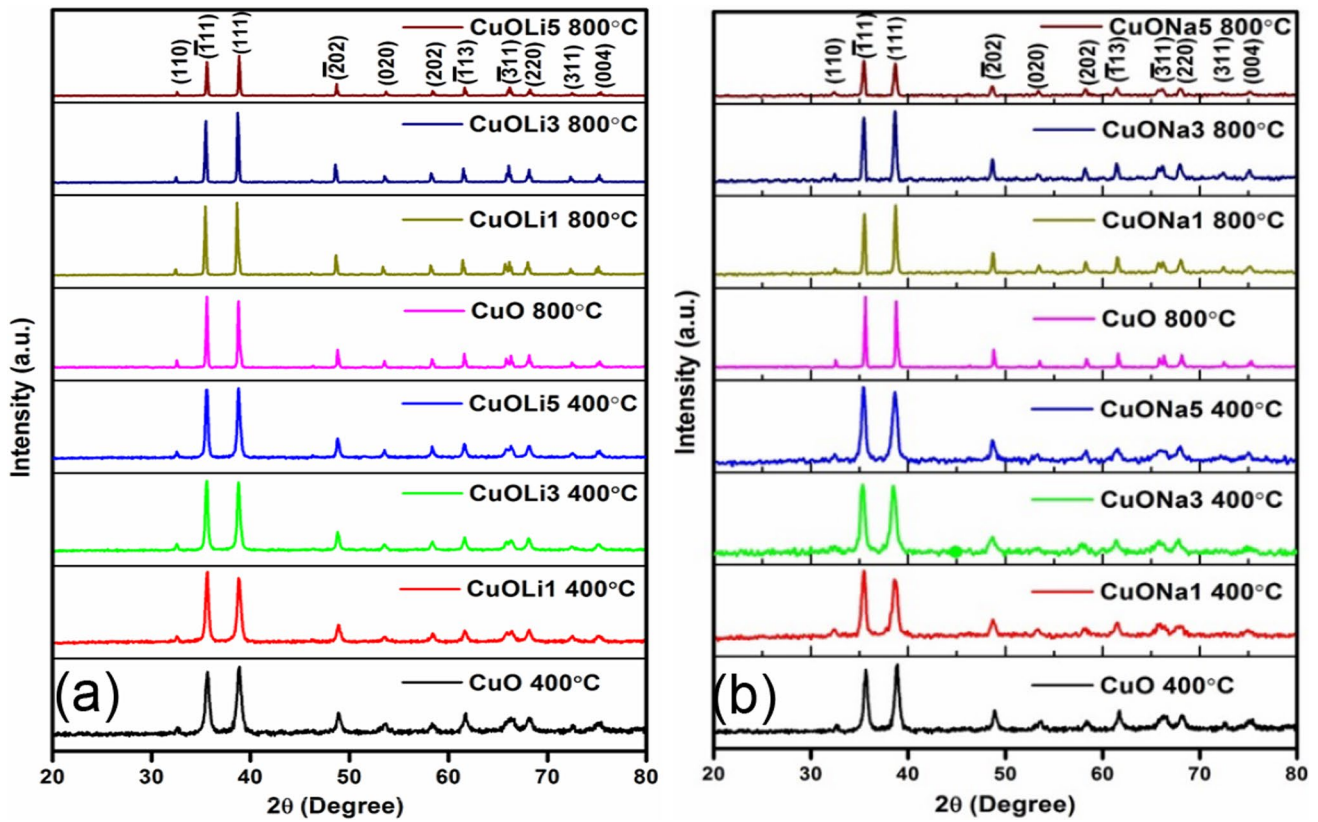
Fig. 1 XRD patterns of as-prepared (400 °C) and 800 °C annealed **a** Li-doped and **b** Na-doped CuO in comparison with undoped CuO of nanostructures

Table 1 Lattice parameter and crystallites size of undoped, and Li- and Na-doped CuO

| Sample	Crystallite size (nm)	Lattice Constant (Å)			Unit Cell Volume (Å³)
		a	b	C	
CuO 400 °C	17.94	4.6718 ± 0.0092	3.4151 ± 0.0043	5.1161 ± 0.0102	80.510
CuOLi1 400 °C	24.52	4.6601 ± 0.0092	3.4177 ± 0.0043	5.1358 ± 0.0102	80.664
CuOLi3 400 °C	29.65	4.6794 ± 0.0092	3.4200 ± 0.0038	5.1273 ± 0.0102	80.907
CuOLi5 400 °C	31.74	4.6773 ± 0.0092	3.4202 ± 0.0038	5.1274 ± 0.0102	80.881
CuONa1 400 °C	27.99	4.6984 ± 0.0107	3.4334 ± 0.0038	5.1391 ± 0.0150	81.738
CuONa3 400 °C	23.23	4.7016 ± 0.0034	3.4561 ± 0.0034	5.1323 ± 0.0034	82.253
CuONa5 400 °C	20.22	4.6950 ± 0.0048	3.4454 ± 0.0038	5.1216 ± 0.0053	81.706
CuO 800 °C	59.80	4.6683 ± 0.0053	3.4202 ± 0.0034	5.1363 ± 0.0087	80.879
CuOLi1 800 °C	57.08	4.7282 ± 0.0160	3.4278 ± 0.0034	5.1113 ± 0.0209	81.663
CuOLi3 800 °C	62.06	4.7123 ± 0.0204	3.4175 ± 0.0048	5.1373 ± 0.0262	81.531
CuOLi5 800 °C	68.57	4.6804 ± 0.0043	3.4101 ± 0.0034	5.1301 ± 0.0048	80.710
CuONa1 800 °C	71.13	4.7039 ± 0.0150	3.4252 ± 0.0034	5.1262 ± 0.1070	81.429
CuONa3 800 °C	57.45	4.6953 ± 0.0053	3.4396 ± 0.0038	5.1305 ± 0.0087	81.702
CuONa5 800 °C	53.18	4.6889 ± 0.0034	3.4377 ± 0.0034	5.1327 ± 0.0038	81.558
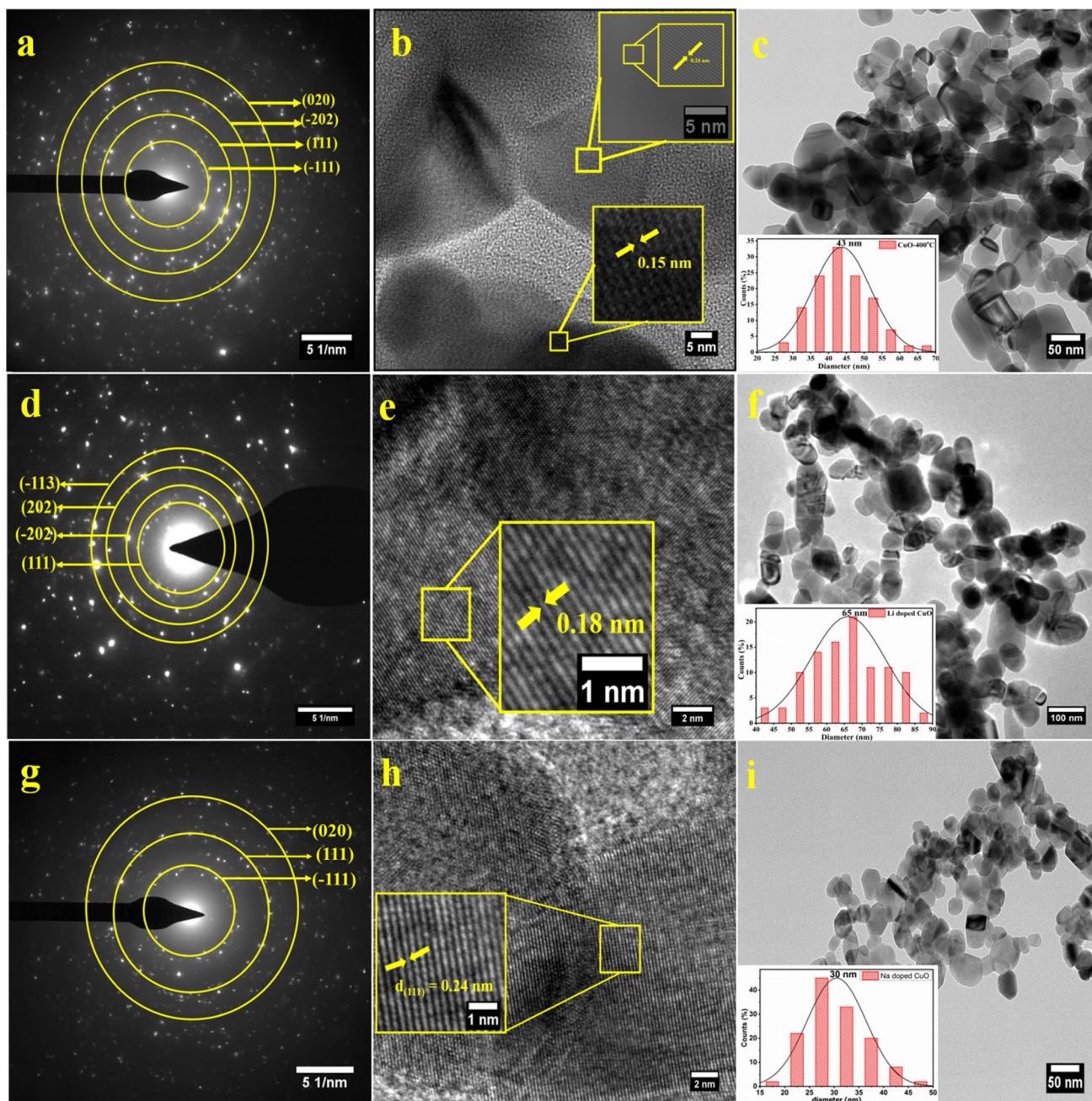
Fig. 2 SAED pattern, HRTEM *d*-spacing pattern, and low magnification particle images of (**a–c**: top) CuO 400 °C, (**d–f**: middle) CuOLi3 400 °C and (**g–i**: lower) CuONa3 400 °C.

to the nanostructures. The diffraction peaks were indexed according to JCPDS card numbers 89-5895 [30]. The average crystallite sizes *D* (nm) were calculated using Scherrer's formula [31] given by,

$$D = \frac{k\lambda}{\beta\cos\theta}, \tag{1}$$

where *k* = shape constant, *λ* = wavelength, *β* = FWHM, and *θ* = angle at which the diffraction occurs. Table 1 lists the average crystallite sizes of CuO, Li-doped CuO, and Na-doped CuO nanoparticles. This reveals a variation in the crystallite growth of Li-doped and Na-doped as-prepared (400 °C) CuO nanostructures. Upon annealing (800 °C), the crystallite growth was significantly increased for

the Li-doped samples whereas the crystallite size decreased for Na-doped samples. Na ions inhibit the crystallite growth due to the small ionic radii of Cu compared to Na. The calculated average crystallite size of as-prepared Li-doped CuO increased from 24 to 32 nm and from 57 to 68 nm for the 800 °C annealed samples. An enhancement in the crystallite size of Li-doped CuO arises from the ionic radius difference of lithium (0.59 Å) and copper (0.73 Å) in the tetrahedral coordination. The increase may be due to the higher ionic mobility, lower activation energy, and small radius of the Li ions. During the growth process, the induced lower activation energy initiates the easy transfer of Li ions to the nucleation sites that lead to the crystallite size increase than that of the trap sites. The lattice constant variations imply the presence of lattice defects owing to forces exerted by Li ions, especially lattice strain [20, 30].

The lattice constants c of the Na-doped CuO larger than those of the undoped signifies the incorporation of the Na ions into substitutional positions. It is believed that the substitution of larger Na^+ (1.02 Å) with smaller Cu^{2+} (0.73 Å) increases the lattice constant [33]. The peak intensities increased marginally upon Na doping which could perhaps be due to the occupation of Na at oxygen vacancies [34] (antisite). As the doping concentration increases, the peak intensities become more intense and sharper indicating good crystallinity. No additional peaks related to secondary and impurity phases owing to the dopant of Li as well as Na ions are observed. All the parameters confirmed the presence of an alkali atom in the CuO lattice.

Structural information further obtained from HRTEM and SAED analysis are presented in Fig. 2 for CuO-400 °C, CuOLi3-400 °C, and CuONa3-400 °C nanostructures. All the samples confirm the polycrystalline features of CuO nanostructures. The SAED concentric ring patterns indicate the Bragg reflection planes with their inter-planar spacing of 0.15 nm, 0.18 nm, and 0.24 nm for undoped, Li-doped, and Na-doped samples, respectively, and match well of the relevant planes, crystalline nature without any additional phase and corroborate well with the XRD analysis. The low magnification HRTEM image indicated that the nanoparticles are structurally uniform of spherical shape morphology with overlapping grains and the particle sizes are in the range of 15–90 nm with an average of 43 nm, 65 nm, and 30 nm for undoped, Li-doped and Na-doped samples, respectively. The particle size variation and d-spacing increase manifest the dopant incorporation as well as the concentration and different ionic radius of Li and Na in the Cu site or as interstitial in the lattice. The TEM resolved higher particle size tendency is comparable to the crystallite size from XRD and the size variation is due to the crystallites agglomerations due to multiple domains combining to form a particle leading to an increase in particle size owing to their difference in dopant ionic radii and concur with the XRD discussions above.
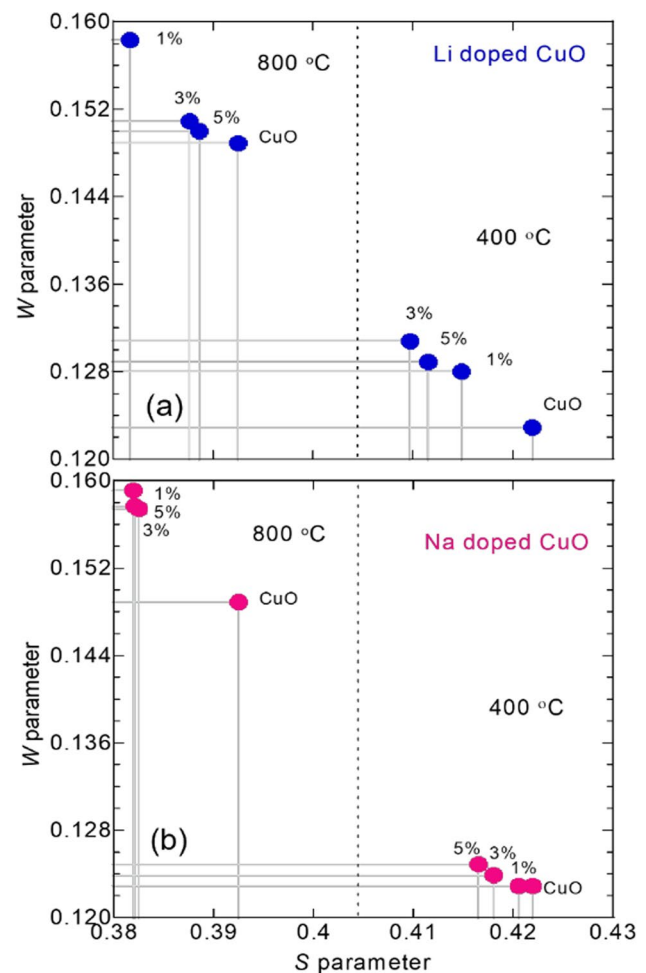

Fig. 3 S-W plot of **a** Li- and **b** Na-doped CuO (solid line to guide the eyes and the dashed line to distinguish as-prepared (400 °C) and 800 °C samples

3.2 Positron Doppler broadening studies

The electron momentum distribution changes in the DBAR spectra are expressed by the S–W parameter to quantify the defects. The S and W parameters variations reflect the changes due to the annihilation of positron–electron pairs with low-momentum and high-momentum electrons, respectively. S parameter increase/decrease together with the W parameter decrease/increase or both parameters increase/decrease indicates the variation in vacancy size and concentration. Figure 3 depicts the variation in S and W parameters of 400 °C as-prepared and 800 °C annealed undoped, Li-doped CuO and Na-doped CuO. Comparing the undoped CuO, Li (1% and 3%)-doped CuO exhibits a decrease in the S parameter that demonstrates reduced vacancy concentrations, thereby indicating the Li ions occupied the existing Cu vacancies and adjust the oxygen vacancies to compensate for the charge neutrality [35]. The S

parameter increase for the 5% doping may be due to the partial amount of Li-ion occupied at the grain boundaries. The increase and decrease of S and W clearly show the changes in defect concentration resulting in doping. Whereas, in all the Na-dopant concentrations the S parameter decreases with a small increase in W, indicating the defect size reduction with lesser defect concentration and significantly differs from Li-doped CuO. As the dopant Na ionic radius is higher than Cu^{2+}, it tends to occupy the grain boundary and hence reducing the crystallite size [36, 37]. This effected with a marginal decrease of S with Na concentration that indicates a reduction in defect concentration.

For the 800 °C annealed Li-doped CuO, the S parameter is considerably reduced than for the as-prepared 400 °C samples. This trend clearly explains that Li^+ trapped at the surface of the grain boundaries further migrates and occupies the Cu vacancy site. Moreover, the Li ions also migrate to the lattice and could occupy the interstitial position on annealing. The S parameter increases for the 3% and 5% Li dopant concentration compared to the Li 1% dopant. The non-linear variation of the S/W parameter and the significant decrease of the S parameter compared to undoped CuO show the increased annihilations with the Cu 3d electrons, while in the case of the O vacancy, the W parameter changes are minimal. This may be an indication of a point defect presence such as a neutral oxygen vacancy. On the other hand, the S decreases due to the migration of Na into the CuO lattice from the surface, thus recovering vacancy defects at 800 °C. Annealing at a higher temperature leads to a reduction of Cu vacancies in the CuO lattice. The difference in ionic radii makes it difficult to occupy a Cu vacancy of the as-prepared sample. So, there are no substantial changes in the S and W parameters for 400 °C Na-doped samples. This may be possible

at high-temperature annealing for Na with a compressive stress field since Na is 29% bigger than Cu [38]. Hence, Na ions migrate to the vacancy site to reduce Cu vacancy-type defects. When Na ions occupy the substitution site, lattice distortion may occur, resulting in lattice stress resulting in a slight decrease in W for Na-doped samples. The slight decrease could be due to the occupation of oxygen vacancies by Na ions [39] where a Na atom may incorrectly occupy a site on the O sublattice (antisites defect). When compared to the CuO annealed sample, the S/W is linearly reduced/increased and hence, the V_{cu}–V_o vacancies recovered in Na-doped samples (Fig. 3).

3.3 Positron lifetime studies

The positron lifetime spectrum was resolved into three components τ_1, τ_2, and τ_3 for all samples and presented in Table 2. The shortest positron lifetime (τ_1) is in the range of 154–228 ps with intensities of 35–51% for as-prepared samples and ascribed to the annihilation in the free state. The τ_1 variations also include the Bloch state residence time of trapped positrons in defects [40] that comprise structural defects in the crystallite and on the surface [41]. An intermediate lifetime τ_2 is due to the defect species component originating from the annihilation of positrons at vacancy clusters in the grain interface. The ortho-positronium pick-off annihilation from free-volume such as microvoids that existed in the grain junction is accounting from the long lifetime component τ_3 with intensity I_3 corresponding to the microvoids concentration [41, 42]. In nanocrystalline materials, the majority of positrons get trapped and annihilated in the grain boundaries that act as positron trapping centers [43, 44]. The diffusion length of positrons in CuO nanomaterials is reported at a maximum of 52 nm [45–47] and higher than

Table 2 Analyzed positron lifetime and DBAR parameters

| Sample	Positron lifetime components						DBAR parameters	
	τ_1 (ns)	I_1 (%)	τ_2 (ns)	I_2 (%)	τ_3 (ns)	I_3 (%)	S	W
CuO 400 °C	0.215 ± 0.005	50.8 ± 2.8	0.377 ± 0.006	48.5 ± 2.8	2.3 ± 0.11	0.7 ± 0.03	0.42196 ± 0.00026	0.12293 ± 0.00012
CuOLi1 400 °C	0.190 ± 0.004	45.4 ± 2.1	0.358 ± 0.004	54.2 ± 2.0	1.9 ± 0.18	0.4 ± 0.04	0.41490 ± 0.00025	0.12799 ± 0.00012
CuOLi3 400 °C	0.154 ± 0.005	39.0 ± 1.8	0.340 ± 0.005	60.2 ± 1.5	0.9 ± 0.13	0.8 ± 0.40	0.40979 ± 0.00026	0.13083 ± 0.00013
CuOLi5 400 °C	0.158 ± 0.004	35.4 ± 1.3	0.354 ± 0.003	64.2 ± 1.2	1.1 ± 0.18	0.4 ± 0.10	0.41150 ± 0.00026	0.12889 ± 0.00013
CuONa1 400 °C	0.217 ± 0.006	40.3 ± 3.3	0.364 ± 0.005	59.2 ± 3.4	2.4 ± 0.10	0.5 ± 0.03	0.42050 ± 0.00026	0.12293 ± 0.00012
CuONa3 400 °C	0.222 ± 0.007	41.5 ± 3.5	0.363 ± 0.005	58.2 ± 3.7	2.5 ± 0.23	0.3 ± 0.02	0.41800 ± 0.00026	0.12385 ± 0.00012
CuONa5 400 °C	0.228 ± 0.005	47.6 ± 3.5	0.368 ± 0.005	52.2 ± 3.6	2.7 ± 0.32	0.2 ± 0.02	0.41646 ± 0.00026	0.12488 ± 0.00012
CuO 800 °C	0.131 ± 0.003	63.2 ± 3.3	269.0 ± 0.013	34.2 ± 2.5	0.6 ± 0.054	2.6 ± 1.01	0.39243 ± 0.00025	0.14891 ± 0.00014
CuOLi1 800 °C	0.147 ± 0.0003	100	–	–	–	–	0.38160 ± 0.00024	0.15830 ± 0.00014
CuOLi3 800 °C	0.160 ± 0.0003	100	–	–	–	–	0.38769 ± 0.00025	0.15086 ± 0.00014
CuOLi5 800 °C	0.164 ± 0.0003	100	–	–	–	–	0.38857 ± 0.00025	0.15004 ± 0.00014
CuONa1 800 °C	0.147 ± 0.003	99.9 ± 0.02	1.1 ± 0.23	0.1 ± 0.03	–	–	0.38205 ± 0.00025	0.15772 ± 0.00014
CuONa3 800 °C	0.146 ± 0.004	99.1 ± 0.09	0.5 ± 0.03	0.9 ± 0.11	–	–	0.38245 ± 0.00024	0.15747 ± 0.00014
CuONa5 800 °C	0.145 ± 0.003	99.7 ± 0.01	2.0 ± 0.11	0.3 ± 0.01	–	–	0.38193 ± 0.00025	0.15913 ± 0.00014
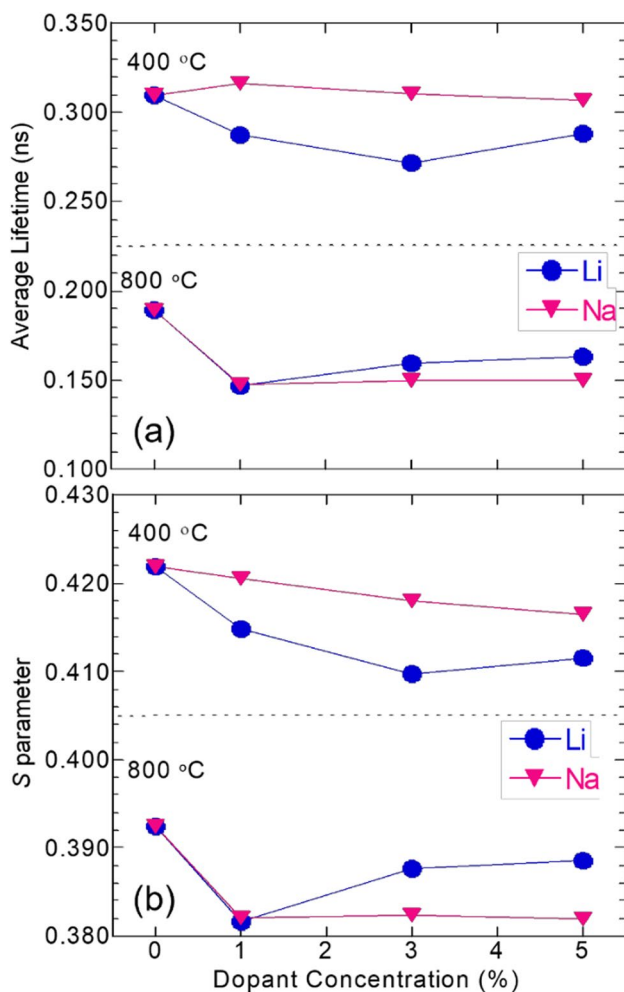
Fig. 4 a Average positron lifetime **b** S parameter of Li- and Na-doped CuO (dashed line is to distinguish 400 °C and 800 °C) samples

the crystallite size of the as-prepared samples indicating the defects.

Figure 4a displays the dopant concentration with the average lifetime calculated using the equation

$$\tau_{ave} = \Sigma \tau_i I_i / \Sigma I_i, \tag{2}$$

where τ_i and I_i are the positron lifetime and its intensity. A gradual decrease in τ_{ave} shows that Li occupies the Cu vacancies and cluster vacancies and for the 5% doped sample, a slight increase indicates the existence of high-concentration point defects. Whereas, as prepared Na-doped CuO samples not featured such variations indicating a possibly occupied grain boundary defect than the presented Cu vacancy. A sharp drop in τ_{ave} for all samples to annealed 800 °C is a clear indication of the reduction in overall defect concentration. The average lifetime is increased for a higher concentration of Li and is almost the same for all Na dopants. This indicates the Li ions localization in the V_{Cu} as well as their

preference to form a point defect with higher Li concentration; whereas, Na ions most likely occupied V_{Cu}. Likewise, the τ_{ave} comparable parameter S variations from DBAR as presented in Fig. 4b also give the overall vacancy defect and concentration. The decrease of S and τ_{ave} for all samples annealed to 800 °C indicates the decrease in the defect species and their comparison gives complementary information. The individual lifetime and their relative intensity for all samples could be examined to confirm a clear understanding of defect dynamics and migration of Li, and Na ions due to annealing.

Figure 5 shows the PAL spectra of as-prepared (400 °C) and annealed (800 °C) Li-doped CuO samples. The reported positron lifetimes of bulk CuO and Cu monovacancy are 169 ps and 230 ps [41] and the bulk lifetime value associated with Cu monovacancy is 180 ps [48]. The first-lifetime component (τ_1) of 216 ps (51%) cannot be assigned to the aforementioned defects only and could be attributed to a mixed contribution from CuO bulk and extended defects in the two-grain interfaces [42, 49]. The second lifetime (τ_2) 377 ps (48%) is attributed to trapped positrons at cluster vacancy defects in the crystallites and grain boundary [50] and is comparable to the V_{Cu}–V_O complexes lifetime [51].

For 800 °C annealed CuO, the intensity I_1 is increased due to the reduction of cluster vacancies (I_2) and micropores concentration (I_3). The shortest τ_1 (130 ps) is down from the bulk lifetime. Since a very small percentage ($< 1\%$) of ortho-positronium is exposed in the sample, the contribution of *para*-positronium (125 ps) with its negligible intensity is also ignored since *para*-positronium may not influence this lifetime [52]. The shortest τ_1 (130 ps) is due to the bulk and associated Cu interstitial (Cu_i) defect. First-principles calculation reported that Cu_i has a stable charge state (Cu_i^0) in the entire range of Fermi levels in an oxygen environment [9]. As a result, the Cu interstitial influences the positron annihilation rate which could be the reason for decreasing the first lifetime. The τ_2 is also reduced to 269 ps owing to the V_{Cu}–V_O complexes reduction to V_{Cu}–V_O vacancy [41]. The significant reduction as well as the size reduction of microvoids are evident in the grain interface and junction of the annealed CuO [42]. The recovery of a Cu vacancy-type defect is prominent in the crystallite.

The first lifetime of 1% Li-doped CuO is 190 ps (45.5%) due to the bulk lifetime value associated with Cu monovacancy in the 400 °C annealed sample. The lifetime value is reduced to 154 (39%) and 159 (35.4%) ps for 3% and 5% Li-doped samples. While the removal of residues at 400 ºC (explained in the experimental section), the vacancies could be migrated and formed as clusters and, hence, the first lifetime is closer to the bulk value. The concentration of cluster vacancies is increased in terms of dopant concentration as evidenced by the intensity I_2. The recovery of Cu monovacancies is not revealed as a function of dopant concentration,
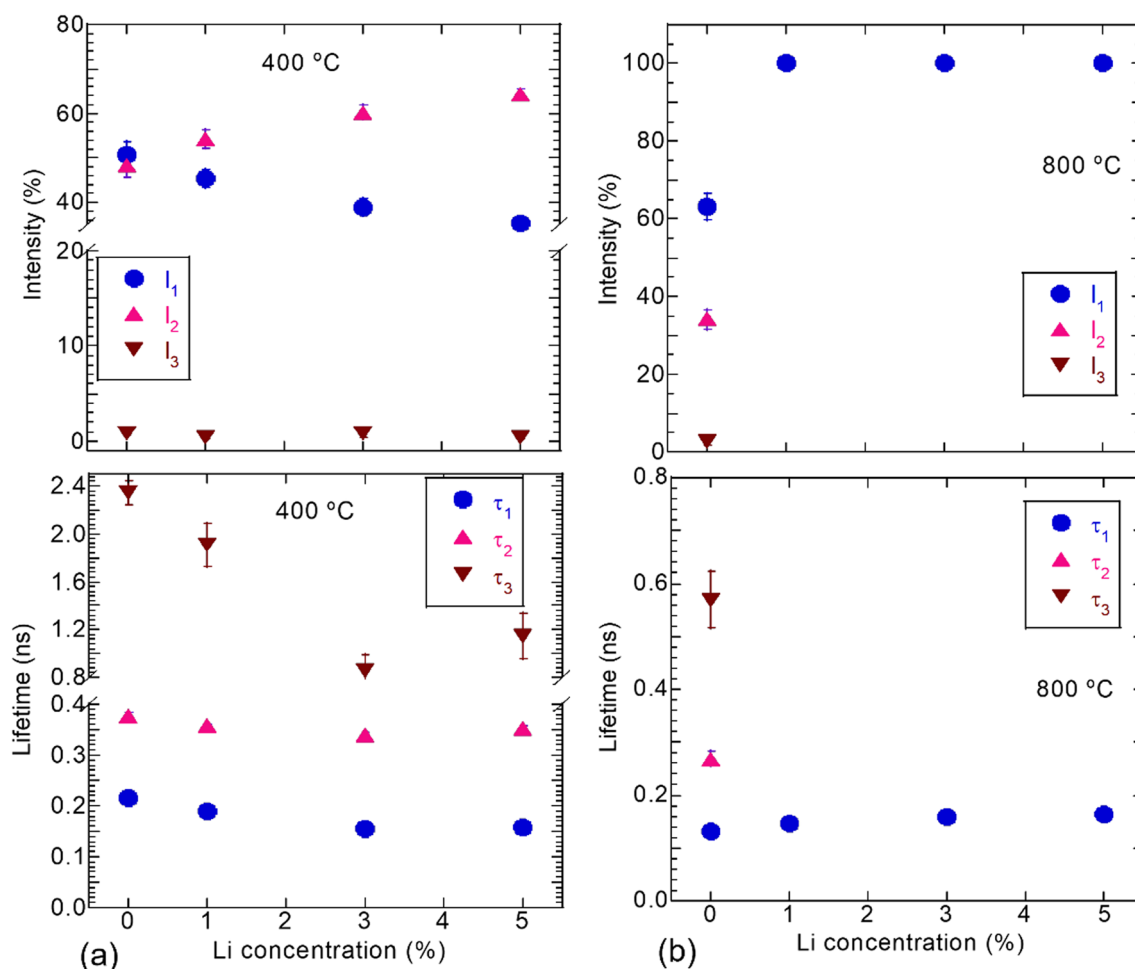
Fig. 5 Positron lifetime and relative intensity of undoped and Li-doped CuO **a** 400 °C and **b** 800 °C

but they are agglomerated and formed as small clusters. Hence, the cluster vacancy concentration (I_2) is increased (54%, 60%, and 64%) with increasing dopant concentration (1%, 3%, and 5%). The *ortho*-positronium lifetime component of doped samples is decreased compared to undoped CuO and their intensity is almost the same for doped samples (<1%).

For a 1% Li-doped 800 °C annealed sample, the first-lifetime component 147 ps less than the bulk lifetime could be due to Li interstitial. All the second and third lifetimes disappeared for 1, 3, and 5% Li-doped samples. Most importantly, the surface defect (second component) in the two-grain junction is vanished due to grain growth and its size is greater than the positron diffusion length. The first lifetime of Li-doped CuO is nearly 160 ps for 3% and 164 for 5% Li$^+$-doped CuO closer to its bulk value indicating the complete recovery of all the vacancy-type defects. The trivial increase in a lifetime may be due to the lattice stress of more inertial Li which may create oxygen vacancy defect with increasing Li concentration. The density of Li interstitial

decreases the lifetime and the oxygen vacancy defects increase the lifetime leading to the balancing of the value and showing nearly the bulk value. The ortho-positronium and cluster vacancy components of Li-doped samples vanished in comparison to undoped annealed CuO, and therefore the intensity I_1 is 100%. As a result, Cu vacancies are recovered completely for 1, 3, and 5% Li$^+$ doped CuO.

Figure 6 shows the analyzed data from the PAL spectra of Na-doped CuO for as-prepared (400 °C) and annealed (800 °C) samples. The first-lifetime value of as-prepared Na-doped CuO is 217, 223 and 228 ps for a 1, 3, and 5% doped sample, respectively. The 1% shows the same value of as-prepared CuO. When adding Na, the extended defect is changed to Cu monovacancies. There is no significant change in the positron lifetime but the microporous concentration I_3 decreases as concentration increases. The vacancies agglomerated and formed clusters for 1 and 3%. The occupation of Na ion in micropores also reduced as cluster vacancies, thus increasing I_2. The high concentration of Na ion (5%) prevents the agglomeration of vacancies to
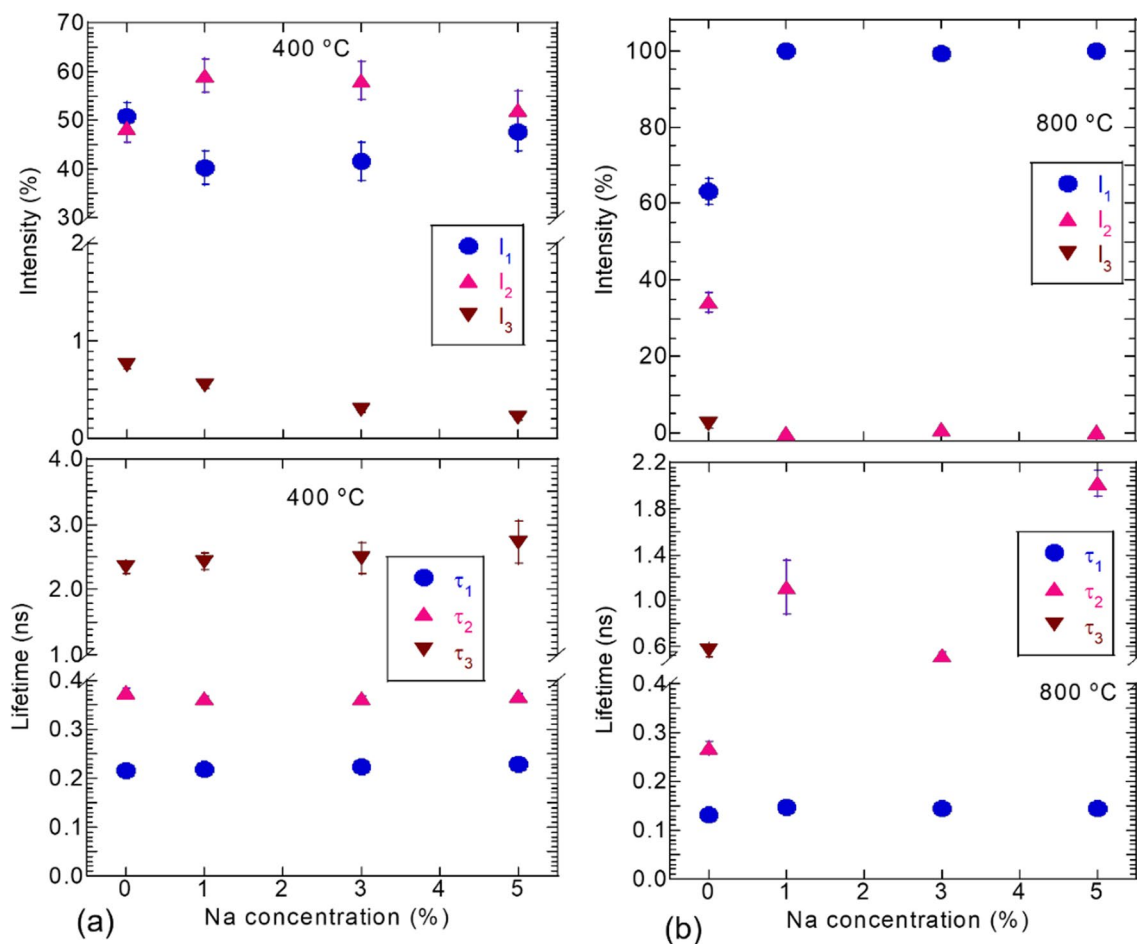
Fig. 6 Positron lifetime and relative intensity of undoped and Na-doped CuO **a** 400 °C and **b** 800 °C

the grain boundary due to Na ion occupied in micropores as evidenced by I_3. There is no change in the first-lifetime values because Na ion could not move to the substitutional positions. The intensity variation is due to Na ions occupied in micropores at the grain boundary junction.

The first-lifetime value of annealed Na-doped CuO is 147, 146, and 145 ps for 1%, 3%, and 5% and their intensity is nearly 100%. The values are almost the same for all dopants but with remarkable changes in the 800 °C annealed sample compared to 400 °C. Na ion tends to move to the substitutional positions, thereby reducing the first-lifetime values. Although Na^+ has bigger ionic radii, the movement of Na ions to Cu substitution positions is possible at high-temperature annealing. The clusters agglomerated as void with a value of less than 1%. Here, a second component is shown as a large value of a big cluster vacancy value, like a small micropore. Annealed sample lifetime revealed that Na substituted for Cu vacancies has not migrated to the interstitial position. This effect is certainly due to the recovery of cluster vacancy defects and the larger fractions of positrons

annihilation in the bulk and revealed nearly 100% intensity. The first lifetime is lower than the bulk value, and it is due to the occupation of oxygen vacancies by Na ion [40] and oxygen interstitial (O_i).

3.4 Comparative analysis of XRD, TEM, Doppler broadening, and positron lifetime

The S parameter and lifetime values distinctly show a reduction of defects. The average lifetime of doped CuO at 800 °C shows clearly that Li and Na ions are occupied in the vacancy, cluster vacancy and open pores. As examined in XRD, the crystallite size was significantly increased with the addition of Li for an 800 °C annealed sample. Likewise, the TEM calculated particle size also increased for 3% doped of the same order as observed in XRD. The positron diffusion fraction into the grain boundary appears to decrease as grain size increases. Most probabilities of positron annihilation in crystallites show that Li-doped CuO has completely reduced the Cu vacancy-type defects, cluster vacancies, and

micropores. The grain growth caused by annealing cures the grain and boundary defect, lowering τ_{av} and S. In contrast, increasing the concentration of Na reduced the crystallite size as well as the particle size significantly because Na ions inhibit grain growth, while the τ_{av} and S parameters remained nearly constant.

Each lifetime component shows very clearly that clusters and voids are recovered for Li and reduced for Na at 800 °C. The concentration of micro void is less than 1% for Na-doped samples. So, the dynamics of vacancy defects and other point defects could be clarified from the first-lifetime component. The vacancies created by replacing Cu^{2+} with alkali metal ions can be understood from the following equation,

$$\left[X_2O \xrightarrow{2CuO} 2X_{Cu}' + V_o^{\cdot\cdot} + O_o^x \right]. \tag{3}$$
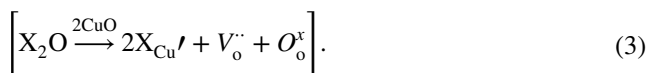
The X^+ ions (Li, Na metal ion) that replace Cu^{2+} ion are considered as negative lattice defects (X_{Cu}'), oxygen vacancies $V_o^{\cdot\cdot}$ as positive defects (2 positive charges) and O_o^x is normal occupied oxygen or anion sites. The charges of one oxygen vacancy are compensated by the charges of two X^+ ions, which will lead to CuO lattice distortion, causing stress [44]. The introduction of charged impurities with a + 1 charge state chemical valence will modify the charge neutrality of Cu. The defect characteristics that change upon the incorporation of Li/or Na ions are determined by charge compensation. The same trend of an average lifetime and S parameter was observed for 1% of Li- and Na-doped samples, but this trend changed with 3 and 5% Li-doped samples. Even though V_{Cu}–V_O vacancies could have been identified for the undoped sample, the V_O^{2+} cannot be identified because positron is rarely trapped. Because positron density concentrates near Cu–O bonds [53] and the shortest distance (1.95) [54], the effects of positron trapping at positively charged vacancies cannot be completely ignored. However, the observed first lifetime of higher Li concentration is not a V_O or V_{Cu} monovacancy lifetime. On the other hand, it cannot be assigned as interstitial, which reduces the lifetime due to the high density of the electron cloud. Since positrons primarily get trapped at negative and neutrally charged vacancies, the first lifetime could be an average value of isolated neutral oxygen vacancy and Li interstitial defects.

Figure 7 shows the ratio of momentum spectra for Li-doped samples concerning CuO-AS (400 °C as-prepared) and CuO-AN (800 °C annealed) samples. The shape of the momentum range (7–30 × 10^{-3}) is the fingerprint of the annihilation with Cu 3d and core electrons [55]. The high intense peak (15 × 10^{-3}) shows the contribution from annihilation from Cu 3d and core electrons for annealed CuO (Fig. 7a); whereas, the low ratio dip shows the contribution from annihilation from 3d electron for as-prepared CuO (Fig. 7b). As

the oxygen vacancies increased, the peak height was down to the momentum range for NiO [56]. It is established that oxygen vacancies are reduced in the oxygen atmosphere annealing [57], thus enhancing the peak amplitude in the momentum range (7–30 × 10^{-3}) for CuO-AN concerning CuO-AS.

Adding Li (1%) also enhances the amplitude over CuO-AN. There is a reduction in further increasing Li concentration for both as-prepared and annealed samples due to increased oxygen vacancies. Oxygen vacancies are a potential source of compensation in Li-doped CuO and the 2 + state ($V_o^{\cdot\cdot}$), to be stable in the Li-doped ZnO crystal annealing out between 500 and 600 K [58]. This state may be varied at high-temperature annealed samples. As the Fermi level moves upward, the thermodynamic charge state transition is, thus, from the 2 + state ($V_o^{\cdot\cdot}$) to the neutral state (V_o). The positive charge state of the oxygen vacancy ($V_o^{\cdot}$) is unstable for any Fermi-level position and also thermodynamically unstable. It is always higher in energy than either ($V_o^{\cdot\cdot}$) or (V_o) for any position of the Fermi level [58]. As previously stated, the positron is rarely trapped in the ($V_o^{\cdot}$) and ($V_o^{\cdot\cdot}$) but possible to initiate trapping less efficiently in neutral vacancy (V_o). When adding more Li impurity, which is in the interstitial position, the valance band minimum may shift upward that increasing the formation energy of the oxygen vacancy in the neutral charge state for the positive charge states. As discussed earlier, for a 1% Li-doped sample, the first lifetime is lower than bulk, and the anion vacancy charge compensation [O^{2-} – X^+ – [$V_o^{\cdot\cdot}$] – X^+ – O^{2-}] may be altered by Li interstitials. Because lifetime confirms the interstitial position of 1% Li, the interstitial Li density at high concentrations could convert the 2 + state to neutral oxygen vacancies. Moreover, Li interstitial density may create the isolated neutral oxygen vacancies needed to relax the lattice strain in the crystallite. The Cu 3d electrons bond with oxygen 2p electrons which are quite delocalized, and their contribution could be in the momentum region of 6–9 × 10^{-3}. The opposed trend of 5% Li compared to 1% Li may be due to localized electrons around the oxygen-neutral vacancies. An opposite trend emerged for the annealed sample in the momentum region of 6–9 × 10^{-3}. This momentum range of 5% Li clearly shows oxygen-neutral vacancies from the momentum ratio to the CuO-AN plot (Fig. 7b). When looking at the momentum plot (Fig. 7a), the oxygen vacancies are generated at a higher Li concentration. Hence, the momentum peak (15 × 10^{-3}) intensity gets decreased with a higher concentration of Li possibly due to isolated oxygen vacancy. The lifetime changes of oxygen-isolated vacancy were larger than bulk and theoretically predicted to be 3 ps [59] and experimentally predicted as 20 ps [60]. In our case, it shows a near bulk value and assumes to be due to the average value of neutral vacancies (V_o) and Li interstitial impurity.
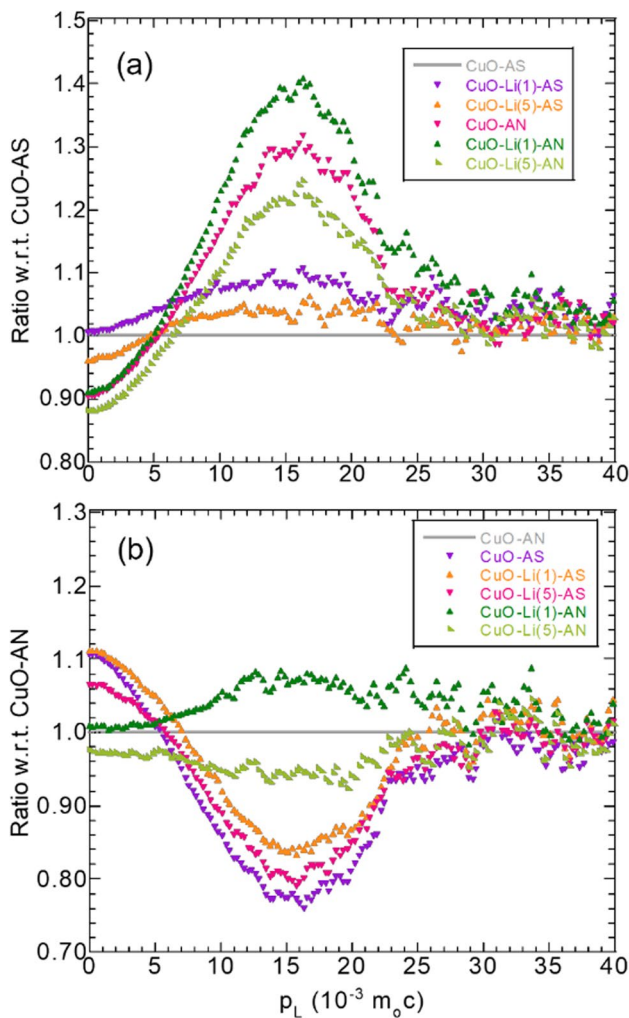
Fig. 7 Ratio plot of momentum spectra for Li-doped samples **a** CuO-AS (400 °C as-prepared) and **b** CuO-AN (800 °C annealed)

Fig. 8 Ratio plot of momentum spectra for Na-doped samples **a** CuO-AS (400 °C as-prepared) and **b** CuO-AN (800 °C annealed)

Figure 8 shows ratio the of momentum spectra for Na-doped samples to CuO-AS (400 °C as-prepared) and CuO-AN (800 °C annealed) samples. Na-doped samples exhibit a similar curve progression but with a slight drop-off and further increases in concentration compared to annealed 1% Na-doped CuO. Although ionic compensation occurs for Na-doped annealed samples, the interstitial regions are less compact. The Na interstitial lifetime may have been less than the Li interstitial because the electron density is more than Li. The lifetime value did not show the interstitial effect for Na-doped samples and showed a recovery of Cu vacancies. The low momentum $(6–9 \times 10^{-3})$ of the annealed Na-doped sample can be attributed to Na occupying oxygen vacancies (antisite defects). The first lifetime could not be affected for a Na-doped sample to concentration. This lower momentum range $(6–9 \times 10^{-3})$ is the positron annihilation in regular occupied oxygen sites. The low momentum range $0–5 \times 10^{-3}$ is the grain boundary curing effect that increases with Li/Na concentration due to annealing.
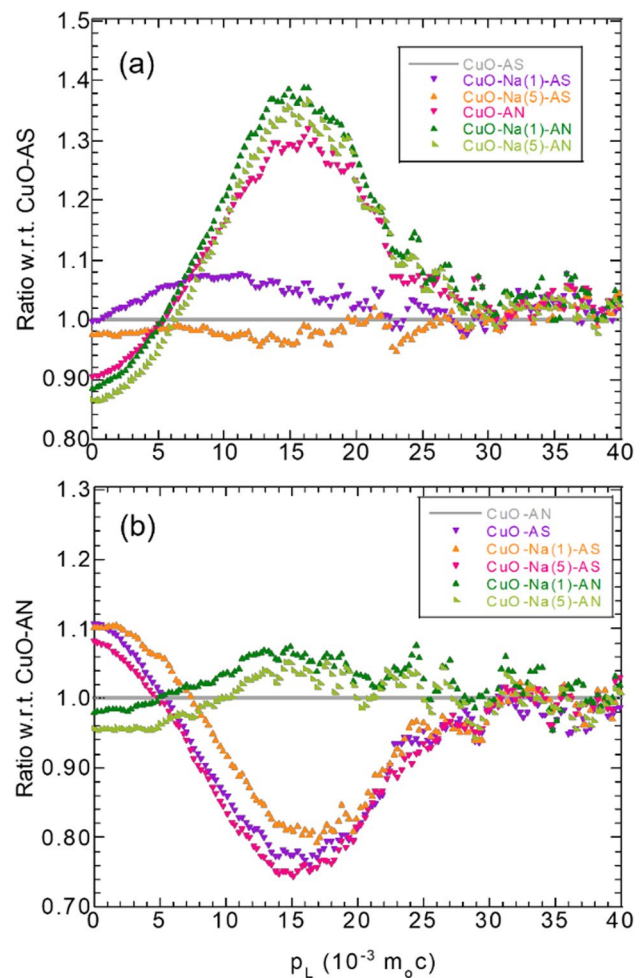
Positron lifetime and momentum variation are due to neutral oxygen vacancies along with Li interstitial and antisite defects along with oxygen interstitial created by Li and Na, respectively. The present study of Li^+ ions occupying the Cu site or V_{Cu} shows improved electrical and thermal properties of a prospective thermoelectric material [7]. In addition, the presence of oxygen vacancies, interstitial Li; antisite and oxygen interstitial take place on Na doping might play a significant role in their electronic properties.

4 Conclusion

XRD and HRTEM analysis of Li/Na-doped CuO nanostructures confirmed the single-phase fine crystalline monoclinic structures, crystallite size variations, grain growth, and grain surface modifications. Positron studies revealed the presence of extended point defects, $V_{Cu}–V_O$ complexes, microvoids

in as-prepared CuO; and the presence of Cu_i defect consequent to annealing. V_{Cu} and cluster vacancies concentration increase for a higher % of Li dopant and their annealing samples signified the formation of Li_i and isolated neutral V_O. Na ion occupied in the grain boundaries further moved in V_{Cu} and possibly in V_O on annealing and signified the formation of antisite defects and O_i. Annihilation with Cu 3d core electrons shows the reduction of V_O and the bonding with oxygen 2p electrons indicates the neutral V_O in $Cu_{1-x}Li_xO$ and O_i in $Cu_{1-x}Na_xO$. The present study contributes to the nature of native point defects and their modification upon doping which will significantly modify the electronic properties.

Data availability The data supporting this study's findings are available from the corresponding author [S. Sellaiyan], upon reasonable request.

Declarations

Conflict of interest The authors declare no conflict of interest in the present work.

References

1. T.H. Tran, V.T. Nguyen, *International Scholarly Research Notices* **2014** (2014)
2. Z.C. Feng, *Handbook of zinc oxide and related materials: volume two, devices and nano-engineering* (CRC Press, Boca Raton, 2023)
3. R. J. Tilley, *Defects in solids*. (John Wiley & Sons, 2008)
4. K. Kim, J. Yu, J. Noh, L.C. Reimnitz, M. Chang, D.R. Gamelin, B.A. Korgel, G.S. Hwang, D.J. Milliron, J. Am. Chem. Soc. **144**, 22941–22949 (2022)
5. A.I.A. Elsharawy, S.M. Yakout, M.A. Wahba, A.A. Abdel-Shafi, M.S. Khalil, Solid State Sci. **139**, 107166 (2023)
6. T. Makino, K. Tamura, C. Chia, Y. Segawa, M. Kawasaki, A. Ohtomo, H. Koinuma, Phys. Rev. B **65**(12), 121201 (2002)
7. N. Yoshida, T. Naito, H. Fujishiro, Jpn. J. Appl. Phys. **52**, 031102 (2013)
8. N. Kumar, D. Sanyal, A. Sundaresan, Chem. Phys. Lett. **477**(4), 360–364 (2009)
9. C.-T. Hsieh, J.-M. Chen, H.-H. Lin, H.-C. Shih, Appl. Phys. Lett. **83**(16), 3383–3385 (2003)
10. Q. Xin, A. Papavasiliou, N. Boukos, A. Glisenti, J.P.H. Li, Y. Yang, C.J. Philippopoulos, E. Poulakis, F.K. Katsaros, V. Meynen, P. Cool, Appl. Catal. B **223**, 103–115 (2018)
11. M. Bibi, Q.-U.-A. Javed, H. Abbas, S. Baqi, Mater. Chem. Phys. **192**, 67–71 (2017)
12. S. Sonia, I.J. Annsi, P.S. Kumar, D. Mangalaraj, C. Viswanathan, N. Ponpandian, Mater. Lett. **144**, 127–130 (2015)
13. A. Yildiz, Ş Horzum, N. Serin, T. Serin, Appl. Surf. Sci. **318**, 105–107 (2014)
14. L.V. Devi, S. Sellaiyan, S. Sankar, K. Sivaji, Mater. Res. Express **5**(2), 024002 (2018)
15. L. Vimala Devi, T. Selvalakshmi, S. Sellaiyan, P. SahayaMurphin Kumar, S. Sankar, J. Mater. Sci. Mater. Electron. **29**, 9387–9396 (2018)
16. A.A. Gvozdenko, S.A. Siddiqui, A.V. Blinov, A.B. Golik, A.A. Nagdalian, D.G. Maglakelidze, E.N. Statsenko, M.A. Pirogov, A.A. Blinova, M.N. Sizonenko, A.N. Simonov, R.B. Zhukov, R.O. Kolesnikov, S.A. Ibrahim, Sci. Rep. **12**, 12843 (2022)
17. S.J. Singh, P. Chinnamuthu, Colloids Surf. A **625**, 126864 (2021)
18. A. Hezam, K. Namratha, D. Ponnamma, Q. Drmosh, A.M.N. Saeed, K.K. Sadasivuni, K. Byrappa, ACS Omega **4**(24), 20595–20605 (2019)
19. J. Sivasankari, S. Sankar, S. Selvakumar, L. Vimaladevi, R. Krithiga, Mater. Chem. Phys. **143**, 1528–1535 (2014)
20. L.V. Devi, T. Selvalakshmi, S. Sellaiyan, A. Uedono, K. Sivaji, S. Sankar, J. Alloy, Compd **709**, 496–504 (2017)
21. S. Sellaiyan, A. Uedono, K. Sivaji, S. Janet Priscilla, J. Sivasankari, T. Selvalakshmi, Appl. Phys. A **122**, 920 (2016)
22. M.J. Puska, R.M. Nieminen, Rev. Mod. Phys. **66**, 841–897 (1994)
23. P.J. Schultz, K.G. Lynn, Rev. Mod. Phys. **60**, 701–779 (1988)
24. M. M. Eldrup, P. Sanders, J. Weertman, *Presented at the Materials Science Forum*, p. 633679 (1997)
25. K. Saarinen, P. Hautojärvi, P. Lanki, C. Corbel, Phys. Rev. B **44**, 10585–10600 (1991)
26. J. Makinen, P. Hautojarvi, C. Corbel, J. Phys. Condens. Matter **4**, 5137 (1992)
27. V.J. Ghosh, B. Nielsen, T. Friessnegg, Phys. Rev. B. **61**, 207–212 (2000)
28. A. Mills Jr., I.O.S. Press, Amsterdam **125**, 209–258 (1995)
29. H. Saito, T. Hyodo, Radiat. Phys. Chem. **68**, 431–434 (2003)
30. L. Vimala Devi, S. Sellaiyan, T. Selvalakshmi, H.J. Zhang, A. Uedono, K. Sivaji, S. Sankar, Adv. Powder Technol. **28**, 3026–3038 (2017)
31. B. D. Cullity, S. R. Cullity, S. Stock, *Elements of X-ray Diffraction* (2001)
32. P. Chand, A. Gaur, A. Kumar, U.K. Gaur, Appl. Surf. Sci. **307**, 280–286 (2014)
33. A. Chelouche, T. Touam, F. Boudjouan, D. Djouadi, R. Mahiou, A. Bouloufa, G. Chadeyron, Z. Hadjoub, J. Mater. Sci. Mater. Electron. **28**, 1546–1554 (2017)
34. B. Sahin, T. Kaya, Appl. Surf. Sci. **362**, 532–537 (2016)
35. S.T. Hossain, E. Azeeva, K. Zhang, E.T. Zell, D.T. Bernard, S. Balaz, R. Wang, Appl. Surf. Sci. **455**, 132–143 (2018)
36. J. Yang, R. Wang, L. Yang, J. Lang, M. Wei, M. Gao, X. Liu, J. Cao, X. Li, N. Yang, J. Alloys Compd. **8**, 3606–3612 (2011)
37. S. Sellaiyan, L. Vimala-Devi, K. Sako, A. Uedono, K. Sivaji, J. Alloys Compd. **788**, 549–558 (2019)
38. L.W. Wang, F. Wu, D.X. Tian, W.J. Li, L. Fang, C.Y. Kong, M. Zhou, J. Alloy, Compd. **623**, 367–373 (2015)
39. E. Şennik, S. Kerli, Ü. Alver, Z.Z. Öztürk, Sens. Actuators B Chem. **216**, 49–56 (2015)
40. R. Siegel, Annu. Rev. Mater. Sci. **10**(1), 393–425 (1980)
41. F. Ameena, Ph.D. thesis, University of Texas at Arlington (2012)
42. R. Pareja, R. De La Cruz, L. Díaz, J. Mater. Sci. **26**(3), 593–596 (1991)
43. M. Majumder, R.B. Choudhary, A.K. Thakur, I. Karbhal, RSC Adv. **7**(32), 20037–20048 (2017)
44. M. Miritello, R. Lo-Savio, A.M. Piro, G. Franzo, F. Priolo, F. Iacona, C. Bongiorno, J. Appl. Phys. **100**(1), 013502 (2006)
45. Y. Tan, Z. Fang, W. Chen, P. He, J. Alloy. Compd. **509**(21), 6321–6324 (2011)
46. T. Jia, W. Wang, F. Long, Z. Fu, H. Wang, Q. Zhang, Mater. Sci. Eng., B **162**(3), 179–184 (2009)
47. H. Li, Z. Zhang, J. Huang, R. Liu, Q. Wang, J. Alloy. Compd. **550**, 526–530 (2013)
48. J. Shi, J. Wang, W. Yang, Z. Zhu, Y. Wu, Mater. Res. (AHEAD) **19**(2), 316–321 (2016)

49. T. Staab, R. Krause-Rehberg, B. Kieback, J. Mater. Sci. **34**(16), 3833–3851 (1999)
50. D. Wang, Z. Chen, C. Li, X. Li, C. Cao, Z. Tang, Physica B **407**(14), 2665–2669 (2012)
51. R.M. De La Cruz, R. Pareja, L. Diaz, J.V. GarcÃ-Ramos, Solid State Commun. **71**(2), 93–95 (1989)
52. D. Biswas, A.S. Das, S. Kabi, L.S. Singh, M. Ahmed, S. Mukherjeee, P.M.G. Nambissan, J. Alloys Compd. **864**, 158395 (2021)
53. P. Turchi, A. Wachs, K. Wetzler, J. Kaiser, R. West, Y. Jean, R. Howell, M. Fluss, J. Phys. Condens. Matter **2**(6), 1635 (1990)
54. J. Ghijsen, L.-H. Tjeng, J. van Elp, H. Eskes, J. Westerink, G.A. Sawatzky, M.T. Czyzyk, Phys. Rev. B **38**(16), 11322 (1988)
55. A. Somoza, M. Petkov, K. Lynn, A. Dupasquier, Phys. Rev. B **65**(9), 094107 (2002)
56. B. Pandey, N. Bhagat, Mater. Res. Express **5**(6), 065030 (2018)
57. D. Gao, J. Zhang, J. Zhu, J. Qi, Z. Zhang, W. Sui, H. Shi, D. Xue, Nanoscale Res. Lett. **5**(4), 769–772 (2010)
58. A. Janotti, C.G. Van de Walle, Phys. Rev. B **76**(16), 165202 (2007)
59. F. Tuomisto, V. Ranki, K. Saarinen, D.C. Look, Phys. Rev. Lett. **91**(20), 205502 (2003)
60. F. Tuomisto, K. Saarinen, D.C. Look, G.C. Farlow, Phys. Rev. B **72**(8), 085206 (2005)